

Accurate Tool Servo Control for Precision Diamond Turning using Heterodyne Interferometry

Kenneth C. Johnson, December 2, 2020

Abstract

The accuracy of precision diamond turning, e.g. for aspheric optics fabrication, can be greatly improved by incorporating dynamic interferometry in the tool position feedback loop. A miniature optical interferometer attached to the cutting tool or tool post measures the displacement between the tool and the workpiece surface, and the interferometer signal controls a fast-servo piezoelectric actuator incorporated in the tool post to minimize mid-spatial-frequency surface machining errors. The interferometer can also dynamically measure the step height across the tool's cutting line to control low-spatial-frequency surface errors, and high-spatial-frequency roughness can be controlled by optimizing the geometry of the tool's cutting edge.

1. Overview

Advanced optical systems for applications such as extreme ultraviolet (EUV) lithography require Angstrom-scale surface form and finish tolerances over apertures up to 1 meter in size. [1] This is well beyond the capability of precision diamond turning (PDT), which typically achieves surface finish and form tolerances of order 1 nm Sa and 100 nm P-V, respectively. [2, 3] High-spatial-frequency surface roughness can be substantially eliminated with polishing, and low-spatial-frequency errors can be corrected with ion-beam finishing, but mid-spatial-frequency errors in the range of approximately 1 μm to 1 mm cannot be easily corrected.

Mechanical ruling engines, which are used to fabricate X-ray diffraction gratings, achieve nanometer-scale surface finish and form tolerances [4], but PDT systems cannot attain that performance level because they lack servo control feedback from surface metrology on the workpiece during cutting operations. This limitation can be overcome by attaching a miniature optical interferometer to the cutting tool, or to the tool post, to measure short-range positional variations (e.g. on the scale of the tool feed pitch or larger), which give rise to mid-spatial-frequency surface roughness. The interferometer's reference beam is retroreflected by a mirror attached to the tool or the tool post, and its sample beam is focused onto and reflected by the workpiece on the uncut surface. The phase interference between the two beams provides a precise measure of the tool position relative to the workpiece. The sample beam's focus spot can be large enough, e.g. up to 1-mm wide, to cover the mid-spatial-frequency range so that the interferometer signal represents the tool displacement relative to a fiducial average surface height with short-range topography variations filtered out.

The interferometer signal controls a fast-servo piezoelectric actuator incorporated in the tool post to stabilize the positional relationship between the tool and workpiece, allowing only slow variations in the cutting depth relative to the fiducial surface position. This process would be used in a trim-cut operation to improve the surface finish of a pre-machined workpiece. The

tool post, with its integrated interferometer and piezo actuator, can operate as an autonomous accessory to the PDT machine, requiring only high-level command and status communication with the PDT control system.

The interferometer can also include a second sample beam, which is focused onto the workpiece surface on the cut surface to provide a dynamic interferometric measurement of the cut's depth (again with short-range topography variations filtered out). The measured depth can be compared to a pre-programmed target depth map over the workpiece surface (e.g. determined from a full-aperture interferometric measurement of the surface prior to turning). The depth measurement can provide feedback to the piezo actuator for controlling low-spatial-frequency surface form errors.

In another design variation, the interferometer can include multiple sample beams (more than two) with their foci distributed, e.g., along a line traversing the cut line on the workpiece. The measured surface heights along the line can be fit to a continuous quadratic function plus a discontinuous step across the cut to define a fiducial surface that includes the base surface curvature without the mid-spatial-frequency topography variations. A minimum of four sample beams would suffice to define the three quadratic coefficients plus the depth of cut. A larger number of tightly focused sample beams could be used for high-resolution surface profile imaging, either for controlling a turning operation or just for in-situ metrology.

High-spatial-frequency roughness on the scale of the tool feed pitch or smaller results primarily from the cutting tool geometry. A single-point diamond tool typically creates a V-groove cut pattern, whereas a radiused tool creates a scalloped topography. A smoother surface can be formed by using a single-crystal diamond tool with a straight cutting edge. The edge is defined by the atomic crystal planes, and the edge length exceeds the feed pitch. The PDT system's B axis would be controlled to keep the cutting edge tangent to the workpiece surface, as well as keeping the interferometer's sample beams aligned at normal incidence to the surface.

Interferometrically-controlled turning could be done as a trim-cut process, typically without cutting fluid, which might interfere with the interferometric measurement. If a cutting fluid is required for tool cooling, liquid nitrogen can be used. On the other hand, the surface finish might be improved by using laser heating of the workpiece [5] (with no coolant fluid) in conjunction with interferometric servo feedback.

In addition to improving the accuracy and quality of PDT, an interferometer-controlled cutting process could enable fabrication structures that are not possible with existing manufacturing technology. One such application would be large-area, diamond-turned EUV or x-ray monochromator gratings, which cannot be post-polished but could be produced by the method described in [4] if the PDT accuracy and surface finish were comparable to ruling engines. Such gratings would be useful, for example, as spectral filters in EUV lithography source collection optics. [6]

2. Single-channel interferometer

An interferometer with the above-outlined functional characteristics can be designed in a variety of ways. One approach, based on acousto-optic heterodyning, is described below. This design could also be useful for applications other than diamond turning, such as general-purpose surface profilometry.

The system components are illustrated in Fig. 1. A laser beam is expanded and collimated by a beam expander (BE) and is directed through an acousto-optic modulator (AOM), which divides the beam into two beams, a zero-order beam and a first-order beam, via Bragg diffraction from a periodic acoustic wave. (Section 4 describes a more practical design variant using two AOM's.) The AOM shifts the temporal frequency of the first order relative to the zero order by an increment equal to the acoustic wave frequency. The laser output is linearly polarized in the direction orthogonal to the plane of Fig. 1, and the two similarly polarized zero- and first-order beams are reflected by a polarizing beam splitter (PBS). They then transmit through a Faraday rotator (FR) and a linear polarizer (POL). The Faraday rotator rotates the polarization direction by 45° , and the polarizer is oriented to transmit the polarized beams without loss. A focusing lens (FL1) focuses the zero- and first-order beams onto two separate focal points, where they are collected by polarization-preserving optical fibers. An aberration corrector plate (ACP1) can be placed close to the focal plane, in the space where the beams are spatially separated, to correct aberrations in the lens or other optical components and achieve stigmatic focusing of both beams. (The aberration corrector is a glass plate with a phase-correcting surface topography, which can be formed using grayscale lithography.)

The optical fibers convey the two beams to a sensor head on the PDT system's tool post, which holds the cutting tool. A focusing lens (FL2) collects the two beams diverging from the fibers and reimages them to two conjugate foci at expanded magnification. A second aberration corrector plate (ACP2) can be used to correct aberrations in FL2. The lens is formed on a glass block, which retroreflects one of the beams (the reference beam) from an internal reference mirror surface (RM) at the beam focus. The other beam (the sample beam) exits the block and is brought to a focus at point F on the workpiece, which retroreflects the beam back into the block. The sample beam's focus spot is on the uncut workpiece surface, adjacent to the cut line. Both retroreflected beams are refocused by FL2 onto the fiber apertures.

The reference beam could alternatively be retroreflected by a mirror at the fiber terminus, rather than transmitting through the glass block. But the Fig. 1 design, with both beam passing through the lens block, substantially matches the beams' path lengths so a relatively low-coherence laser source (e.g. a diode laser) can be used. Also, this minimizes the sensitivity of the beams' relative phase difference to temperature variations or stress in the lens block.

The return beams from the sensor head transmit back through the fibers, ACP1, FL1, POL, FR, and PBS. The polarizer (POL) eliminates any cross-polarization contamination (e.g. from depolarization by reflection at the workpiece). The Faraday rotator (FR) rotates the polarization by an additional 45° on the return path, so that it enters the PBS polarized in the plane of Fig. 1 and transmits through the PBS without reflection.

After transmitting through the PBS, the return beams pass through a beam combiner BC, which coherently recombines the two beams. The combiner is a diffraction grating with a lamellar (rectangular-section) profile, which divides each beam evenly between two diffraction orders, a +1 order and a -1 order. (Some power also goes into other orders.) The zero order from the AOM is split by the BC into +1 and -1 orders, which will be identified as the “(0,0,1)” and “(0,0,-1)” orders, and the AOM’s first diffraction order is similarly split by the BC into +1 and -1 orders “(1,0,1)” and “(1,0,-1)”. (The middle “0” index is a place-holder for multi-channel designs, which are discussed in Section 3.) The combiner’s grating period is twice the AOM’s grating period so that the (0,0,1) and (1,0,-1) orders are coherently superimposed in a single combined beam, which is concentrated by focusing lens FL3 onto a photodetector PD1. The signal level on PD1 varies sinusoidally with time in synchronization with the AOM due to the frequency shift between the two beams, and the signal phase is proportional to the optical path length difference between the reference and sample beams from the AOM to PD1. The (0,0,-1) and (1,0,1) orders are captured by photodetectors PD2 and PD3, which sense the separate beam intensities without coherent interaction. These detectors provide a signal normalization reference, which can compensate for factors such as laser output instability. In addition, the AOM acoustic wave amplitude can be varied to keep the PD2 and PD3 signals in balance, so that the contrast ratio of the PD1 phase signal is maximized.

The zero- and first-order beams exiting the AOM have complex amplitudes proportional to $\exp(i2\pi\nu t)$ and $\exp(i2\pi(\nu + \Delta\nu)t)$, respectively, where t is time, ν is the laser’s temporal frequency in cycle/sec units (1 cycle = 2π radian), and the $\Delta\nu$ is the acoustic wave frequency (which can be positive or negative, depending on which direction the wave is travelling relative to the AOM’s Bragg diffraction direction). The zero order’s complex amplitude on PD1 is $A_0 \exp(i2\pi(\nu t + p_0))$ and the first order’s amplitude on PD1 is $A_1 \exp(i2\pi((\nu + \Delta\nu)t + p_1))$, where A_0 and A_1 are positive real, and p_0 and p_1 are proportional to the respective zero and first orders’ optical path lengths from the AOM to PD1. The intensity signal S_1 on PD1 is proportional to the coherent superposition of these two amplitudes,

$$\begin{aligned} S_1 &\propto \left| A_0 \exp(i2\pi(\nu t + p_0)) + A_1 \exp(i2\pi((\nu + \Delta\nu)t + p_1)) \right|^2 \\ &= A_0^2 + A_1^2 + 2A_0 A_1 \cos(2\pi(\Delta\nu t + p_1 - p_0)) \end{aligned} \quad (1)$$

The signal levels S_2 and S_3 on PD2 and PD3, respectively, are proportional to the uncombined beam intensities,

$$S_2 \propto A_0^2, \quad S_3 \propto A_1^2 \quad (2)$$

The phase p_1 varies in proportion to the workpiece’s surface height offset h from the cutting tool along the surface-normal direction,

$$p_1 = \text{const} - 2h / \lambda \quad (3)$$

where $const$ is a constant and λ is the laser wavelength. (h represents an average surface height over the focused sample beam area, which can be large enough to encompass mid spatial frequencies.) The signal S_1 has the following form (from Eq's. (1) and (3))

$$S_1 \propto A_0^2 + A_1^2 + 2 A_0 A_1 \cos(2\pi(\Delta \nu t + p_c - 2h/\lambda)) \quad (4)$$

where p_c is a constant phase offset. p_c need not be calibrated because a single-channel phase measurement would generally be used only to minimize rapid variations in h associated with mid-spatial-frequency errors. Slow variations in response to the PDT system's servo control are not impeded or controlled by the tool post servo. But with addition of a second interferometer channel, as described in Section 3, the interferometer can be used to accurately control the depth of cut as well as reducing mid-spatial-frequency roughness.

The sensor head and cutting tool are both rigidly attached to a mounting block, which is attached to the tool post body by a piezoelectric actuator interface. Position feedback from the interferometer is used to control the cutting depth via the piezoelectric actuator.

3. Multi-channel interferometer

The above-described interferometer senses the height offset between the cutting tool and a fiducial surface on the uncut workpiece surface. A second interferometer channel can be added to also sense the height offset relative to the cut surface, thereby providing a measure of the step height across the cut line. Additional channels can be added to provide robust measurement on curved surfaces, or to provide high-resolution imaging of the surface topography.

In the multi-channel system, the zero- and first-order beams emerging from the AOM are further divided between the multiple channels by a diffraction grating G in Fig. 1. For a two-channel system, a simple lamellar grating can be used, and with more than two channels G can be a binary Dammann grating. The grating lines are orthogonal to the AOM grating, i.e., parallel to the plane of Fig. 1, so grating G disperses the multi-channel beams out of the plane of the figure. The zero order from the AOM will be divided by G into multiple diffraction orders, with the j -th order being identified as “ $(0, j)$ ”, and after traversing the interferometer the $(0, j)$ order will be split by the combiner BC into $+1$ and -1 orders denoted as “ $(0, j, 1)$ ” and “ $(0, j, -1)$ ”. Similarly, the AOM's first order is diffracted by G into orders $(1, j)$, and are diffracted by BC into orders $(1, j, 1)$ and $(1, j, -1)$.

Each channel has its own reference and sample beams, which are transmitted to the sensor head by a separate pair of optical fibers. Focused beam patterns at the fiber entrance plane are illustrated for several design options in Fig. 2. Each circle represents an individual optical fiber, i.e. the outer perimeter of the fiber cladding. The beams are focused onto the fiber cores. Fig. 2(a) illustrates a basic one-channel design, with two fibers that collect orders $(0, 0)$ and $(1, 0)$ as described in Section 2. In this illustration the AOM's zero order is the reference beam and the first order is the sample beam. Fig. 2(b) shows a two-channel configuration, in

which the first channel uses the -1 diffraction order from G and the second channel uses the +1 order. (Typically, with an even number of channels only odd-numbered diffraction orders from G are used. The other orders have zero or very low diffraction efficiency.) Fig. 2(c) illustrates a 4-channel pattern, using G orders -3, -1, +1, and +3 for channels 1, 2, 3, and 4.

After transmitting through the optical fibers, the multi-channel reference beams are all retroreflected by the reference mirror (RM in Fig. 1). The fiber output apertures for the sample beams can be arranged to provide any desired distribution of illumination points on the workpiece. Some alternatives are illustrated in Fig. 3, which shows the sample beam illumination spots in relation to the instantaneous tool path on the workpiece. Fig. 3(a) illustrates a one-channel illumination spot on the uncut surface just ahead of the cut point. In Fig. 3(b), a two-channel system focuses sample beams to spots on either side of the cut line to provide a measure of the cut step height. (For manufacturing grating structures such as those described in [4] and [6], the spots can be anamorphically focused onto individual grating facets.) Fig. 3(c) is a four-channel configuration with the focus spots arrayed along a line traversing the cut line, and in Fig. 3(d) the four spots are arranged in a skewed matrix pattern. Fig. 3(e) illustrates a 16-channel illumination pattern with tightly-focused sample beams arrayed in a matrix pattern to provide high-resolution topographic imaging detail.

Each return beam is diffracted by the beam combiner BC (Fig. 1), with order (i, j) being split into orders $(i, j, 1)$ and $(i, j, -1)$. Orders $(0, j, 1)$ and $(1, j, -1)$ are coherently superimposed to provide a phase interference signal for channel j . The beams are collected by an array of photodetectors, as illustrated in Fig. 4 in the detector aperture plane for (a) a one-channel system, (b) a two-channel system, and (c) a four-channel system.

A multi-channel interferometer can be calibrated by simultaneously measuring the phase offsets p_c in Eq. (4) for all channels with the interferometer focused on an optical flat, which defines a zero-height reference. (In Eq. (4) $h = 0$ on the reference flat.) With p_c determined, the surface heights h for all channels can be determined from Eq. (4). With a two-channel system, the height difference between the two illumination spots in Fig. 3(b) provides a measure of the depth of cut. A small correction for any slight tilt or curvature of the workpiece surface might need to be applied to the measurement. However, with four channels measuring surface heights along a line, as in Fig. 3(c), the correction can be applied automatically in the measurement algorithm. Denoting the height measurements for channels 1, 2, 3, and 4 as h_1 , h_2 , h_3 , and h_4 , and denoting the corresponding measurement position coordinates along the cross-cut direction as x_1 , x_2 , x_3 , and x_4 , the heights can be fit to a quadratic function of x with a discontinuous height drop d across the cut,

$$\begin{aligned}
 h_1 &= a x_1^2 + b x_1 + c \\
 h_2 &= a x_2^2 + b x_2 + c \\
 h_3 &= a x_3^2 + b x_3 + c - d \\
 h_4 &= a x_4^2 + b x_4 + c - d
 \end{aligned} \tag{5}$$

(Channels 1 and 2 are focused on the uncut surface, and channels 3 and 4 are focused on the cut surface with the height differential d , as illustrated in Fig. 3(c).) Eq's. (5) are solved for the unknown quadratic coefficients a , b , and c , and the depth of cut d :

$$\begin{aligned}
 a &= \frac{(h_1 - h_2)(x_3 - x_4) - (h_3 - h_4)(x_1 - x_2)}{(x_1 - x_2)(x_3 - x_4)(x_1 + x_2 - x_3 - x_4)} \\
 b &= \frac{h_1 - h_2 - a(x_1^2 - x_2^2)}{x_1 - x_2} \\
 c &= h_1 - x_1(a x_1 + b) \\
 d &= -h_3 + c + x_3(a x_3 + b)
 \end{aligned} \tag{6}$$

The x coordinates are the beam centroid locations, and each h measurement represents a weighted average surface height over one of the sample beams, with the weighting determined by the beam's diffraction-limited illumination profile. The minimum x spacing is determined by the optical fiber center spacing and the lens FL2 magnification (Fig. 1). However, the x spacing can be reduced by staggering the focus spots as illustrated in Fig. 3(d). A large number of tightly-focused beams, in a staggered pattern as in Fig. 3(e), can be used to acquire a high-resolution raster image of the surface topography.

In the above-described design configurations the reference beams all reflect off of the reference mirror RM in Fig. 1, and the sample beams all reflect off of the workpiece. However, it might be advantageous to have both the reference and sample beams for at least one interferometer channel reflect off of RM. In principle, this "double-reference" channel should read a constant, time-invariant phase. Any variation in the measured phase is likely due to errors in the optics, detectors, or electronics, which similarly affect other channels. The double-reference channel can be used to correct these errors.

4. Acousto-optic modulator design options

The Fig. 1 design uses a single AOM to separate the reference and sample beams. A limitation of the single-modulator design is that a very high acoustic wave frequency $\Delta\nu$ might be required to achieve high Bragg diffraction efficiency and also to achieve a sufficiently large separation angle between the reference and sample beams. Heterodyne interferometers generally use two AOM's to frequency-tune both the reference and sample beams and better control their frequency difference. The AOM's are typically in separate beam paths, which are branched by a beam splitter, but the interference measurement could be impacted by vibrations or temperature variations in the two paths.

These effects can be minimized by replacing the single AOM in Fig. 1 with two in-line modulators illustrated as AOM1 and AOM2 in Fig. 5. AOM1 divides the laser power approximately evenly between angularly separated reference and sample beams, as described in Section 1 (or it controls their power balance to optimize signal contrast at the detectors). For example, the zero order can be used as a reference beam, which will have the same frequency ν as the laser after transmission through AOM1. The first diffraction order is used as a sample

beam, which is frequency-shifted to $\nu + \Delta\nu_1$ by AOM1, where $\Delta\nu_1$ is the acoustic frequency of AOM1. The beams then both transmit through AOM2, which is tuned to efficiently diffract one of the beams, e.g. the reference beam, which will be frequency-shifted to $\nu + \Delta\nu_2$, where $\Delta\nu_2$ is the acoustic frequency of AOM2. But due to the angular selectivity of Bragg diffraction the sample beam is substantially undiffracted by AOM2, so its frequency is unchanged. The frequency difference between the sample and reference beams is therefore $\Delta\nu = \Delta\nu_1 - \Delta\nu_2$, which can be much smaller than $\Delta\nu_1$ and $\Delta\nu_2$.

In the Fig. 5 configuration, AOM1 deviates the diffracted (sample) beam by angle θ_1 , and AOM2 deviates the diffracted (reference) beam by angle θ_2 . The angles are additive, so the two beams will emerge from the second AOM with deviation angle $\theta = \theta_1 + \theta_2$. Alternatively, the diffraction geometry can be arranged as in Fig. 6 so that the angles are subtractive: $\theta = \theta_1 - \theta_2$. In both the Fig. 5 and Fig. 6 configurations the acoustic gratings' Bragg grating planes for both AOM1 and AOM2 are orthogonal to the plane of the figure and the beam directions are all parallel to the plane of the figure before, between, and after the modulators. However, the inter-beam angle can also be controlled by positioning one or both modulators with their Bragg planes in some other orientation, not perpendicular to the figure plane.

References

- [1] S. Migura, "Optics for EUV lithography," in *2018 EUVL Workshop*, P22, EUV Litho, Inc., <https://www.euvlitho.com/2018/P22.pdf>
- [2] Precitech product information (2020), <https://www.precitech.com/>
- [3] Moore Nanotechnology Systems product information (2020), <https://nanotechsys.com/>
- [4] F. Siewert et al., "Gratings for synchrotron and FEL beamlines: a project for the manufacture of ultra-precise gratings at Helmholtz Zentrum Berlin", *J. Synchrotron Rad.* 25, 91–99 (2018). <https://journals.iucr.org/s/issues/2018/01/00/x15026/x15026.pdf>
- [5] Shahinian, Hossein, et al. "Micro laser assisted machining (μ -LAM) of precision optics." *Optical Fabrication and Testing*. Optical Society of America, 2019. <https://doi.org/10.1117/1.OE.58.9.092607>
- [6] K. Johnson, "EUV Source Optics with 100% OOB Exclusion", in *2018 EUVL Workshop*, P14, EUV Litho, Inc., <https://www.euvlitho.com/2018/P14.pdf>

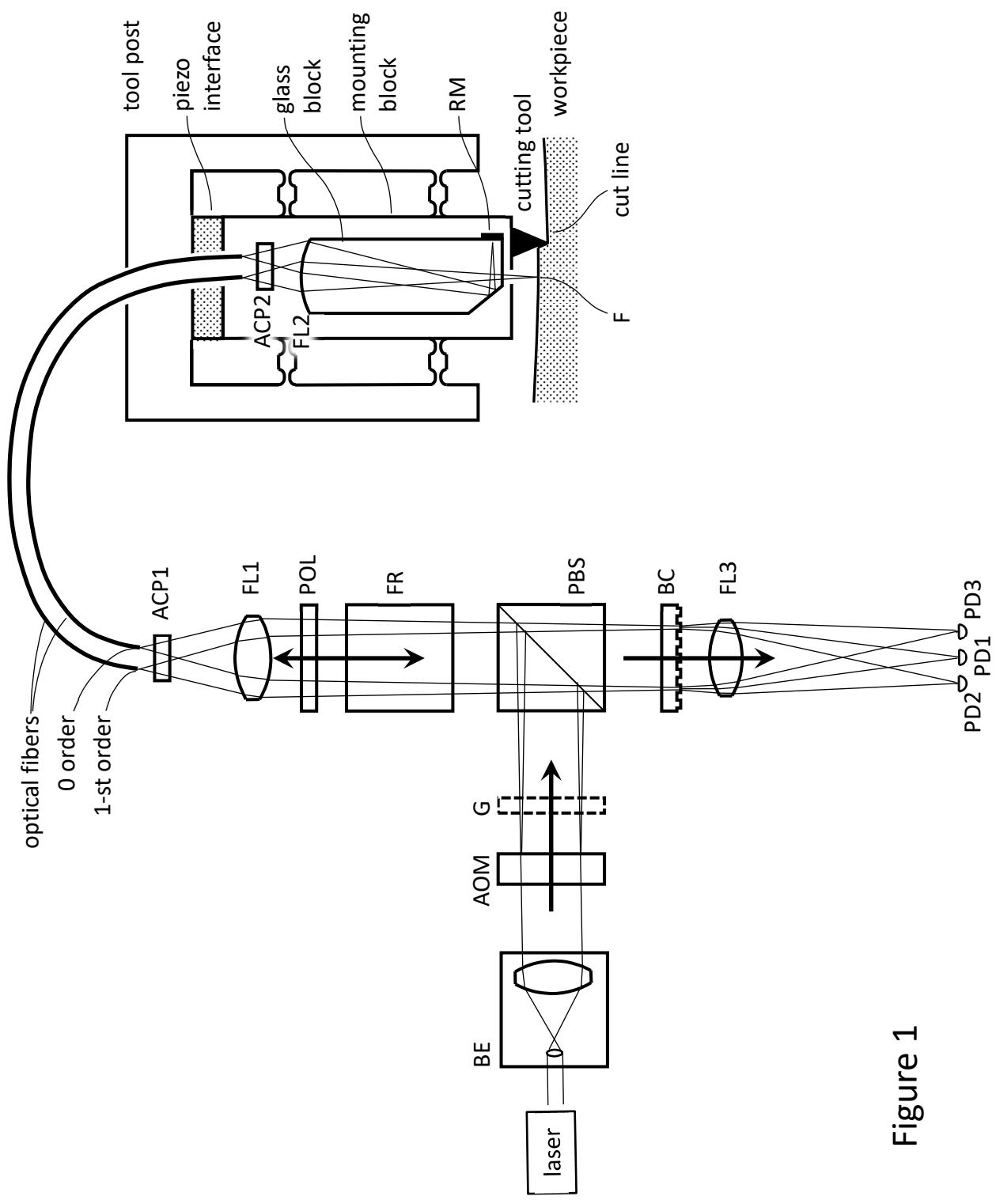


Figure 1

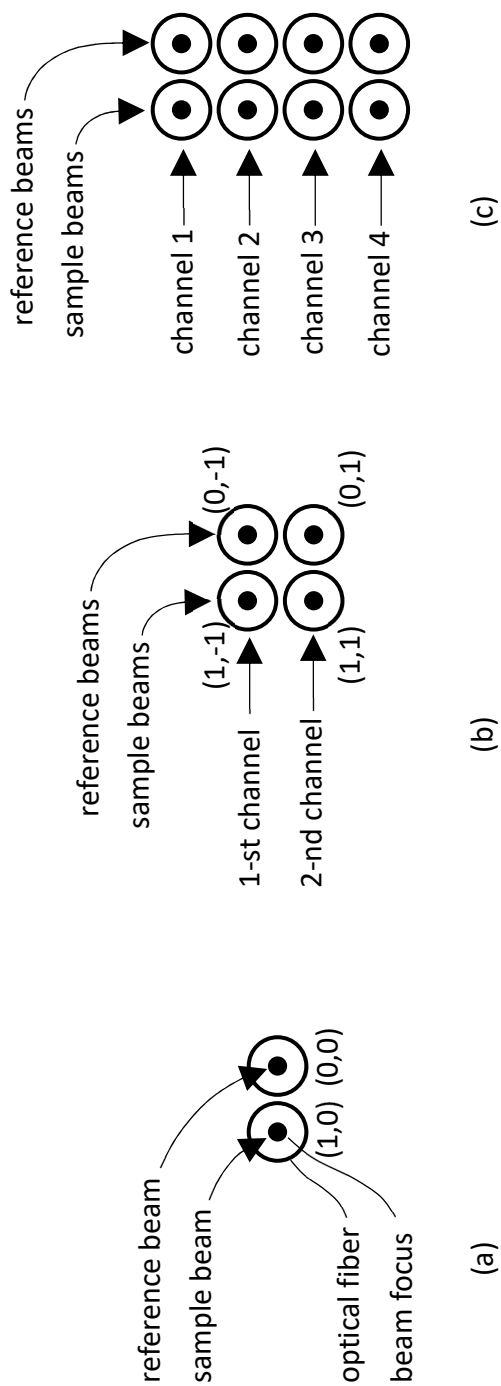


Figure 2

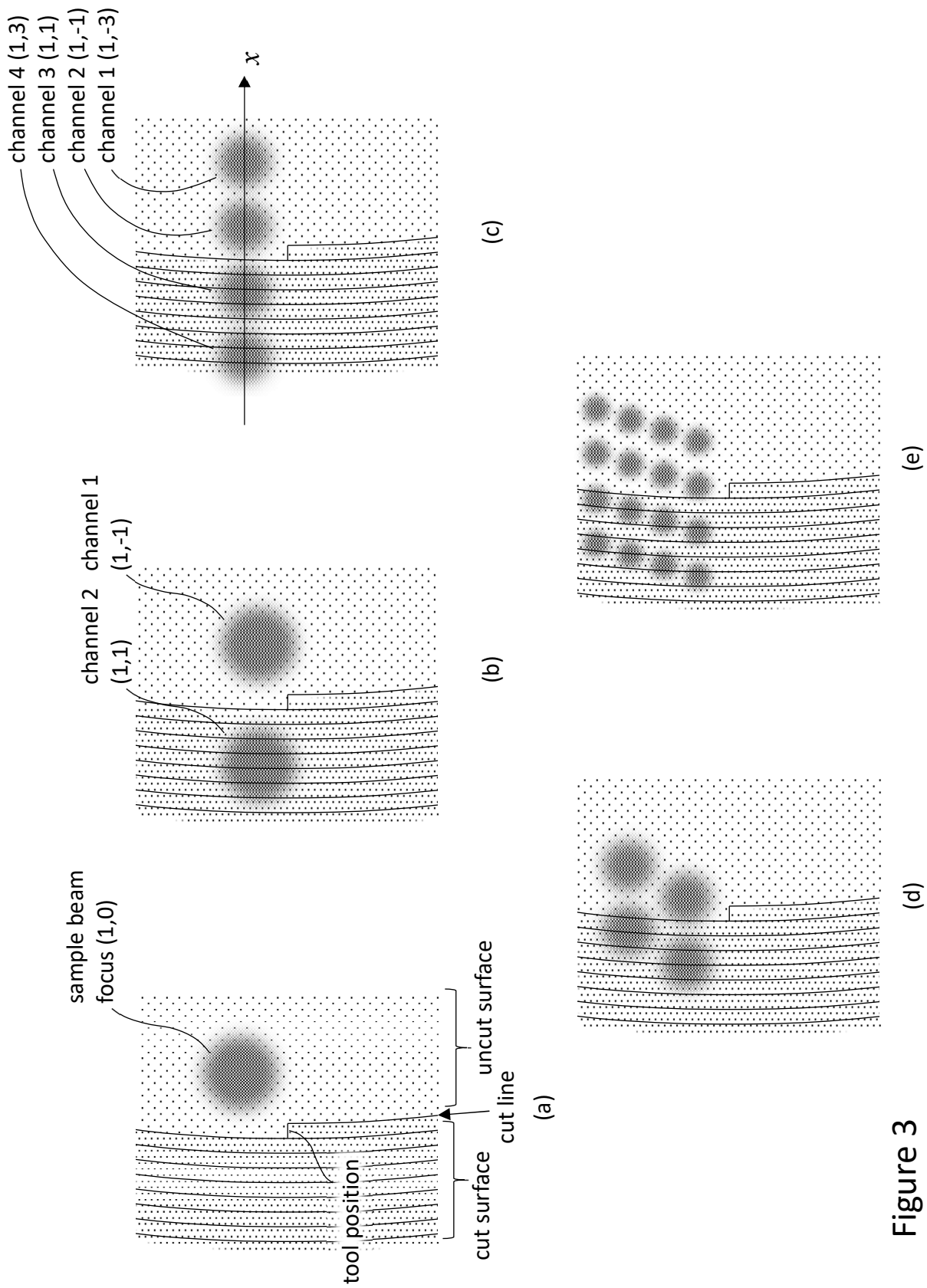


Figure 3

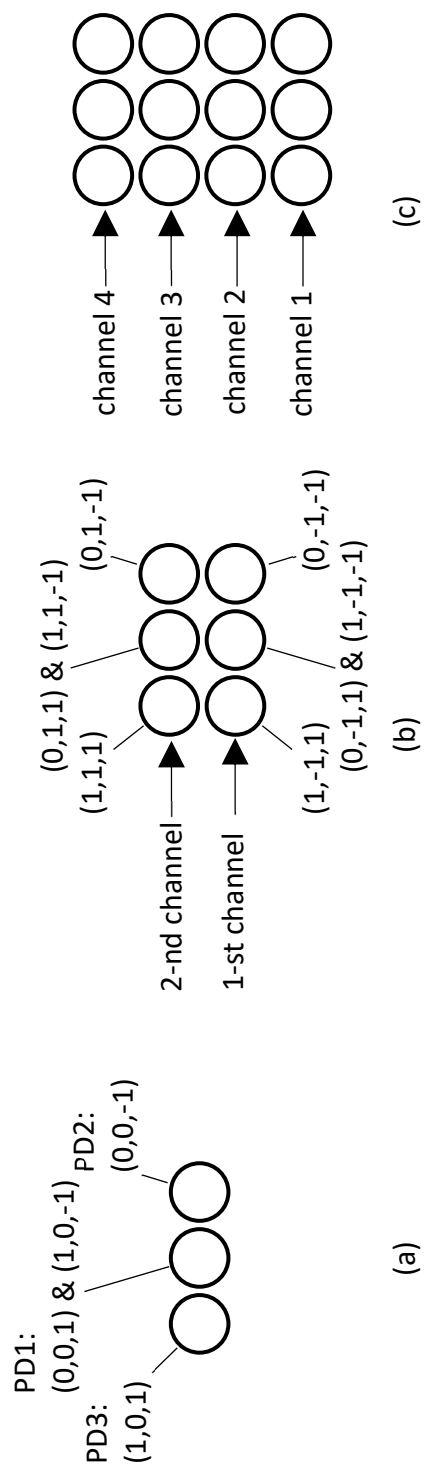


Figure 4

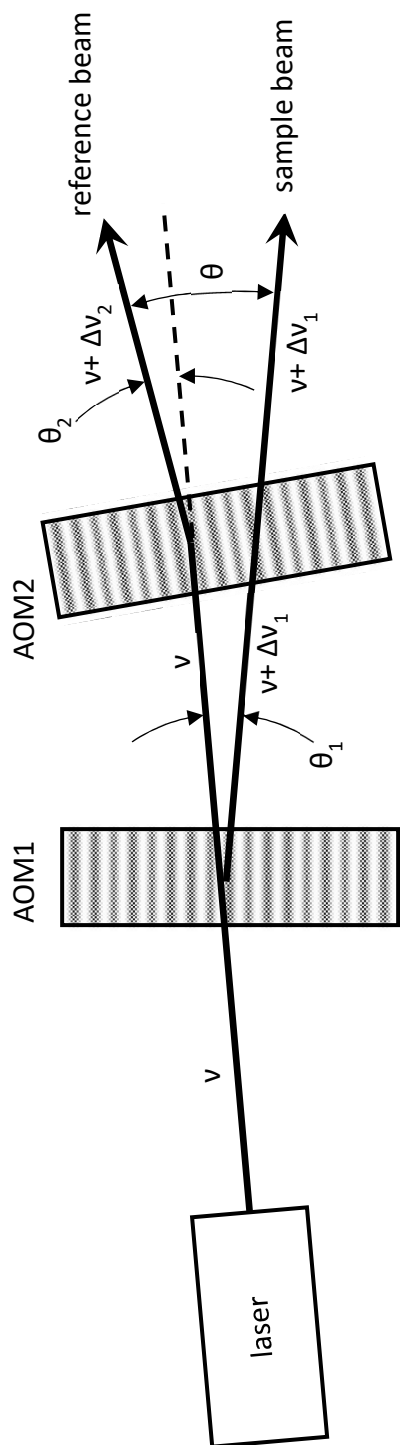


Figure 5

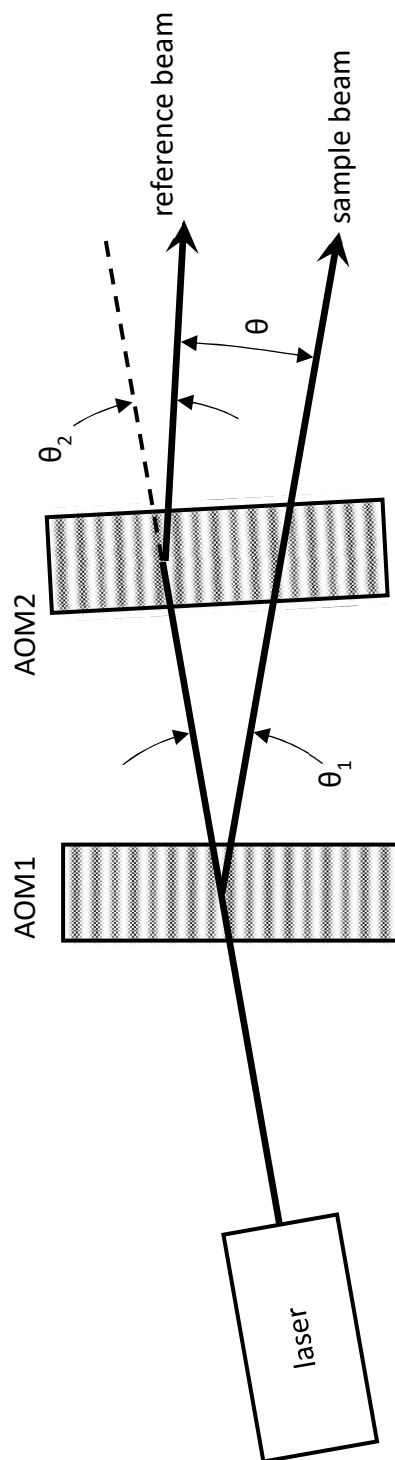


Figure 6